

Lithium abundances and extra mixing processes in evolved stars of M67 $\star, \star\star$

B. L. Canto Martins^{1,2}, A. Lèbre², A. Palacios², P. de Laverny³, O. Richard² C. H. F. Melo⁴,
J. D. do Nascimento Jr¹, and J. R. De Medeiros¹

¹ Universidade Federal do Rio Grande do Norte, Departamento de Física, 59072-970 Natal, RN, Brazil
e-mail: brunocanto@dfte.ufrn.br

² Université Montpellier II, CNRS, UMR 5024, Groupe de Recherche en Astronomie et Astrophysique du Languedoc, Place E. Bataillon, 34095 Montpellier, France

³ Université Nice Sophia Antipolis, CNRS, UMR 6202, Observatoire de la Côte d'Azur, Laboratoire Cassiopée, BP 4229, 06304 Nice, France

⁴ European Southern Observatory, Garching, Germany

Received May 2010, Accepted December 2010

ABSTRACT

Aims. We present a spectroscopic analysis of a sample of evolved stars in M67 (turn-off, subgiant and giant stars) in order to bring observational constraints to evolutionary models taking into account non-standard transport processes.

Methods. We determined the stellar parameters (T_{eff} , $\log g$, $[Fe/H]$), microturbulent and rotational velocities and, Lithium abundances (A_{Li}) for 27 evolved stars of M67 with the spectral synthesis method based on MARCS model atmospheres. We also computed non-standard stellar evolution models, taking into account atomic diffusion and rotation-induced transport of angular momentum and chemicals that were compared with this set of homogeneous data.

Results. The lithium abundances that we derive for the 27 stars in our sample follow a clear evolutionary pattern ranging from the turn-off to the Red Giant Branch. Our abundance determination confirms the well known decrease of lithium content for evolved stars. For the first time, we provide a consistent interpretation of both the surface rotation velocity and of the lithium abundance patterns observed in an homogeneous sample of TO and evolved stars of M67. We show that the lithium evolution is determined by the evolution of the angular momentum through rotation-induced mixing in low-mass stars, in particular for those with initial masses larger than $1.30 M_{\odot}$ when at solar metallicity.

Key words. (Stars:) Stars: abundances – Stars: fundamental parameters – Stars: atmospheres – Stars: evolution

1. Introduction

The investigation of the lithium (Li) abundance in different stellar sites - such as open clusters - is a key element in the study of the chemical evolution of the Galaxy (D'Antona & Matteucci 1991). Regarding the formation of light elements, unlike beryllium (Be) and boron (B), which are formed only via spallation reactions involving protons or alpha particles and atoms of carbon, nitrogen, and oxygen (Reeves, Fowler & Hoyle 1970), lithium is mostly produced during Big Bang nucleosynthesis. Because they are easily destroyed at low temperature in deep stellar layers, these light elements and especially Li provide strong constraints to test transport mechanisms in stellar interiors.

According to standard stellar evolution, where no mechanisms for the transport of matter is included in the radiative regions, the only episode modifying the surface abundance pattern of low-mass stars during their ascent of the Red Giant Branch (RGB) is the first dredge-up (1st DUP) occurring at the base of the RGB. At this stage the convective envelope deepens

and the ashes of hydrogen burning, mainly CN-cycle products, are dredged-up to the stellar surface, causing the decrease of the $^{12}\text{C}/^{13}\text{C}$ and $^{12}\text{C}/^{14}\text{N}$ surface ratios. The regions reached by the convective envelope are also lithium free and the surface lithium abundance therefore drops significantly. The importance of these variations depends on metallicity and initial mass.

However, the large number of abundance anomalies detected in main-sequence and giant stars are evidence pointing to one or more processes of extra-mixing occurring in the stellar interiors (Pinsonneault, 1997). Several extra-mixing processes were suggested with the intention of explaining the Li depletion in F and G type stars: microscopic diffusion (Michaud 1986; Chaboyer et al. 1995), meridional circulation and hydrodynamical turbulent instabilities (Schatzman & Baglin 1991; Pinsonneault et al. 1991; Deliyannis & Pinsonneault 1997; Talon & Charbonnel 1998; Palacios et al. 2003), internal gravity waves (García López & Spruit 1991; Montalbán & Schatzmann 2000; Talon & Charbonnel 2003). However, the physical parameters that control this extra-mixing are subjects of debate (Charbonnel & Balachandran 2000). Among the candidates, rotation-induced mixing alone (Palacios et al. 2003) or associated to internal gravity waves (Talon & Charbonnel 2003) appears to explain the hot and the cold side of the Li-dip observed for main-sequence stars in open clusters. Going beyond the turn-off, Palacios et al. (2003) showed that the same models that reproduce the hot side

Send offprint requests to: B. L. Canto Martins

* Based on observations collected at ESO, Paranal, Chile (VLT/FLAMES program ID 072.D-0309 and 074.D-0179).

** Table 6 is only available in electronic form at <http://www.edpsciences.org>.

of the Li-dip lead to the observed dispersion of Li abundances in subgiants of open clusters and of the galactic field. Concerning the RGB, abundance variations observed at the surface of stars beyond the 1st DUP indicate the existence of extra mixing processes at this stage (Recio-Blanco & de Laverny, 2007). However, rotation-induced mixing does not seem to play a major role in more advanced evolutionary stages, when the rotation decreases because of the increase of the stellar radius, as shown in Palacios et al. (2006) for globular cluster RGB stars. Finally let us mention that the second and third dredge-up episodes that occur during the Asymptotic Giant Branch phase once again modify the surface abundance patterns, and that in these phases abundance anomalies also indicate the action of an extra-mixing process that is not yet clearly identified. Li depletion also seems to be related to the stellar age (Herbig 1965; Duncan 1981; Soderblom 1983; Fekel and Balachandran 1993), and it is also sometimes considered to be connected with other parameters such as metallicity, activity, and mass (Pallavicini et al. 1987; Spite & Spite 1982; Randich et al. 1994). If the Li depletion is related to the stellar age, one could expect a correlation between lithium abundance and rotational velocity for stars of the same mass, same metallicity and same spectral type (Skumanich 1972). In agreement with this, Zahn (1992) and Pinsonneault et al. (1990) postulated that the Li depletion in late-type stars is directly related to the loss of angular momentum.

The age of clusters and consequently that of their individual stars can be determined from isochrone fitting. Cluster stars may therefore more efficiently serve for the study of changes in mixing-sensitive abundances and for the search of anomalies in chemical compositions. Open clusters are moreover important laboratories, from the study of which one can address the question of Li evolution in stellar interiors and surfaces, because they contain a significant sample of stars in a wide range of mass with the same origin and same initial chemical composition. In the last decades several observational diagnostics have discovered element abundances of stars belonging to open clusters of different ages with the help of high-resolution spectroscopy, and even more recently with the multi-objects instruments. The evolution of Li and Be abundances along specific parts of the colour-magnitude-diagrams (CMD) of open clusters (main-sequence, turn-off (hereafter TO), subgiant and red giant branch) has been investigated to test the physics and the extra-mixing processes included in stellar evolution models. Randich et al. (2002 & 2007) have investigated both Be and Li abundances in late-F and early-G main-sequence and subgiant stars from five different open clusters with ages ranging from 50 Myr up to 4.5 Gyr. They confirmed shallow mixing in stellar interiors, which is able to transport surface material deep enough for Li burning to occur, but not deep enough for Be burning. Very recently, Smiljanic et al. (2010) have analysed Be and Li abundances along the main sequence and RGB in the open cluster IC 4651 (with an age estimated around 1.5 Gyr). They show that both the evolution and dispersion of Be and Li abundances are successfully reproduced by theoretical predictions from hydrodynamical models taking into account non-standard mixing processes (rotation-induced mixing, atomic diffusion, and thermohaline mixing).

The present study focusses on evolved stars of the open cluster M67 (= NGC 2682), which has been used for the past three decades as an important laboratory for studying stellar evolution (Burstein et al. 1986; Carraro et al. 1996, and references therein). M67 is commonly mentioned as a solar

age cluster, i.e. one of the oldest open clusters of the Galaxy. However, its age is still a matter of debate, and estimates vary from 3.5 to 4.5 Gyr. A recent estimate (Sarajedini et al., 2009) based on the comparison of a M67 proper-motion-cleaned colour-magnitude diagram to theoretical isochrones points to low values around 3.5 - 4.0 Gyr, confirming previous results from VandenBerg & Stetson (2004) or Michaud et al. (2004), who used evolutionary models taking into account microscopic processes such as atomic diffusion. On the other hand, spectroscopic studies devoted to stars from M67 usually refer to a higher age of about 4.5 Gyr (e.g., Randich et al. 2006). Using spectroscopy and photometry, several authors determined an average iron abundance [Fe/H] for M67 very close to the solar value.

Previous Li observations in M67 stars show that a real dispersion in the lithium abundance of main-sequence objects exists even though at this phase the convective envelope is too superficial to reach the layer where Li destruction can occur (Pasquini et al. 1997; Jones et al. 1999; Randich et al. 2002; 2007). While standard models appeared inefficient to explain this Li dispersion observed in unevolved M67 stars, the rotational mixing seems to be a good candidate (Pasquini et al. 1997). Considering M67 subgiants, Sills & Deliyannis (2000) also find that stellar models with slow mixing caused by rotation are the most suitable to explain the evolution of low-mass stars. By measuring rotational velocities for 28 stars from the main-sequence to the giant branch in M67, Melo et al. (2001) provided an analysis of the history of the angular momentum of stars of $1.2M_{\odot}$. It verifies that these velocities probably obey different laws for the evolution of the angular momentum on the main-sequence and on the giant branch.

Our observations of M67 stars along an evolutionary sequence from the TO to the top of the RGB offers the opportunity to shed light on the interplay between Li and rotation evolution and to test the extra-mixing scenario in stellar structures. In Section 2 we present the observational data and our method to determine stellar parameters (effective temperature, surface gravity, metallicity), Li abundances, and rotational velocities ($v \sin i$). In Section 3 we present the stellar models we used to study the Li evolution in evolved stars of M67, and our conclusions are drawn in Section 4.

2. Spectroscopic observations and data analysis

Our study is based on a sample of 28 post-main-sequence stars of the open cluster M67. Figure 1 displays a colour-magnitude diagram of the open cluster M67 (photometry from Montgomery et al., 1993). We overplotted a best-fitting isochrone of 3.7 Gyr provided by VandenBerg (private communication) based on the models with diffusion by Michaud et al. (2004).

These stars are divided into three groups regarding their evolutionary stages: (i) TO stars, (ii) subgiant branch stars, and (iii) RGB stars, including three clump giants. According to a standard evolutionary scenario, TO and subgiant stars must present a fast expansion of their convective envelopes, while giant stars must have passed already through the first dredge-up episode, bringing to the surface CNO products, hence modifying the surface abundances. Let us mention that among our sample is the Li-rich subgiant S1242, which we analysed in detail in Canto Martins et al. (2006).

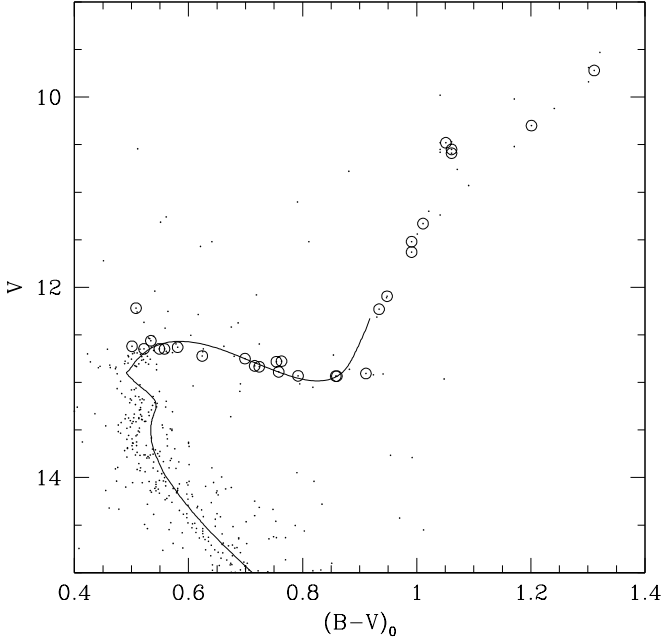


Fig. 1. Colour-magnitude diagram of the open cluster M67. (V , $B - V$) photometry is taken from Montgomery et al. (1993) and a colour excess of $E(B - V) = 0.05$ has been assumed, as in Melo et al. (2001). Stars from our sample are shown as open dot circles. The track is an isochrone at 3.7 Gyr from Vandenberg (private communication) based on models with diffusion from Michaud et al. (2004).

2.1. Spectroscopic observations

The observations of these stars were carried out with the VLT/Unit2 ESO telescope (Paranal, Chile), using the FLAMES-UVES spectrograph (Pasquini et al. 2002), during January 2004, January 2005 and March 2005. Using photometry and astrometry data of M67 from EIS pre-FLAMES (Momany et al. 2001) we selected our stars near the centre field with $\alpha = 8 : 48$ and $\delta = +11 : 46$. We used two different fiber configurations. For the brightest stars ($V < 12$, i.e., RGB stars) we observed four stars, with four fibers dedicated to the sky with the exposure time set to 1 500 sec, providing a mean signal-to-noise ratio (S/N) of 50 (per pixel), over the lithium region (6 700 - 6 720 Å). For the faintest stars ($V > 12$, TO and subgiant stars), seven fibers were used for the stars and one for the sky. The exposure time for these groups was set to 1 500, 2 580, and 3 000 sec, providing a S/N between 65 and 100 (per pixel). The stellar sample was observed with the UVES red arm centred at 580 nm, covering a wavelength range of 420-680 nm, and also centred at 860 nm, covering a larger wavelength range of 660-1 060 nm. The observations have a resolving power of $R \sim 47\,000$ (1 arcsec sky aperture). Moreover, some stars (marked in Table 1 with a star) we only observed with the UVES red arm centred at 580 nm.

The spectra were reduced with the standard FLAMES/UVES data reduction pipeline following the usual steps of reduction (bias, flat-field, and background corrections, order fiber definition, wavelength calibration of the spectra with a ThAr spectrum and extraction of the spectra). Concerning the sky subtraction, for bright stars, four fibers were allocated for the sky on each

plate. The average of the sky fibers was subtracted from each star spectrum. However, for the faintest stars only one fiber was dedicated to the sky and then subtracted from the star spectrum. Then we used IRAF to normalize them to a pseudo continuum and to bring the reduced spectra to rest. The radial velocities for our stellar sample were calculated with the IRAF `fxcor` task. The stellar spectra were cross-correlated with a spectrum of the Sun (Hinkle et al. 2000). The shifts were then computed into radial velocities of the stars and heliocentric correction was applied. The results are presented in Table 1 and the errors in these velocities show a stability at a level of a few hundreds of m/s.

The probability that these stars belong to this stellar cluster is larger than 70%, according to Sanders (1977) and their estimated radial velocities should be consistent with the estimated radial velocity for M67 of 33.0 km s^{-1} (Friel & Janes 1993). This is not the case for the star S1000 with 0% of membership probability and a radial velocity of 42.8 km s^{-1} , which is very different from the group of stars and is therefore rejected.

Finally, we also combined different exposures collected at different dates for some TO and subgiant stars, in order to reach a good quality of the data and to increase the mean S/N over the Li region to 100 per pixel.

A complete log of observations is presented in Table 1. Star identifiers are from Sanders (1977). The radial velocity correction that was applied is mentioned in the last column (which agrees very well with the values produced by Melo et al. 2001).

2.2. Spectral synthesis

We performed spectral synthesis analysis on our 27 sample stars, to derive stellar parameters (T_{eff} , $\log g$, ξ , $[\text{Fe}/\text{H}]$) and to measure rotational velocities and lithium abundances. We used the MARCS models of stellar atmospheres (Gustafsson et al. 2008), which are based on plan-parallel and spherical models at local thermodynamical equilibrium (LTE). The turbospectrum spectral synthesis tools (Alvarez & Plez 1998) and interpolation routines on model atmospheres were used. Solar abundances were taken from Asplund, Grevesse & Sauval (2005) and the collisional damping treatment was performed based on the work of Barklem et al. (Barklem et al. 2000a,b; Barklem & Piskunov 2003, Barklem & Aspelund-Johansson 2005). To compute synthetic spectra, we took taken into account atomic (see below) and molecular line lists: TiO (Plez 1998), VO (Alvarez & Plez, 1998), and CN and CH (Hill et al. 2002).

In order to improve the precision on the atmospheric parameters and on the Li abundances ($A_{\text{Li}} = \log\left(\frac{n_{\text{Li}}}{n_{\text{H}}}\right) + 12$) presented in Canto Martins et al. (2007), we analysed our sample using the curve-of-growth method, which is based on the measurement of equivalent widths (EWs) of a large number of iron lines present in our FLAMES-UVES observations. Indeed, weak features (mainly caused by the Fe I line at 6 707.44 Å) are known to blend the Li line (at 6 707.78 Å), which is used to derive A_{Li} . Hence, a very good precision on the estimate of the Fe abundance and on all atmospheric parameters is required to ensure a determination of A_{Li} with a high accuracy.

To do so, we first calibrated the oscillator strength values ($\log gf$) of 92 Fe I and 14 Fe II spectral lines issued from the

Table 1. Log of the spectroscopic observations of our 28 sample stars. The stars were observed using two different setups, except for those marked with (\star), which were only observed using the setup centred at 580 nm (see text).

Sanders ID	V	(B-V)	α_{2000}	δ_{2000}	Julian Day + 2453000	Exposure time (sec)	v_{rad} (km.s $^{-1}$)
S774	12.93	0.85	08:50:49.93	11:49:12.90	009.74	3000	33.5
					011.77	1500	34.2
					031.76	3000	34.0
					032.76	3000	33.6
					033.64	3000	34.0
S806	12.78	0.81	08:51:00.17	11:54:32.10	009.74	3000	33.4
					011.77	1500	34.3
					031.76	3000	34.0
					032.76	3000	33.6
					033.64	3000	34.0
S978	9.72	1.37	08:51:17.48	11:45:22.70	008.77	1500	34.7
					008.79	1500	34.6
S1000*	12.84	0.78	08:51:23.83	11:47:16.20	382.73	2580	42.8
					382.76	2580	42.9
S1010	10.48	1.11	08:51:22.81	11:48:01.80	008.77	1500	34.1
					008.79	1500	33.8
S1016	10.3	1.26	08:51:17.11	11:48:16.30	008.77	1500	34.6
					008.79	1500	34.4
S1034	12.65	0.61	08:51:18.55	11:49:21.70	028.74	3000	34.6
					028.78	3000	34.6
					033.69	3000	34.8
					033.73	3000	34.9
S1074	10.59	1.12	08:51:12.68	11:52:42.20	007.76	1500	34.2
					007.78	1500	34.7
S1231	12.93	0.92	08:51:29.38	11:45:27.80	009.74	3000	32.9
					011.77	1500	33.6
					031.76	3000	33.5
					032.76	3000	33.1
					033.64	3000	33.5
S1239	12.75	0.76	08:51:44.03	11:46:24.60	028.74	3000	32.8
					028.78	3000	32.9
					033.69	3000	33.2
					033.73	3000	33.2
					033.73	3000	33.2
S1242	12.72	0.68	08:51:36.04	11:46:33.70	009.74	3000	37.5
					011.77	1500	38.4
					031.76	3000	34.1
					032.76	3000	34.4
					033.64	3000	35.1
S1245	12.93	0.92	08:51:44.77	11:46:46.20	028.74	3000	33.1
					028.78	3000	33.1
					033.69	3000	33.3
					033.73	3000	33.4
S1254	11.52	1.05	08:51:45.08	11:47:46.00	007.76	1500	32.9
					007.78	1500	33.5
S1268	12.65	0.58	08:51:49.97	11:49:31.40	009.74	3000	32.7
					011.77	1500	33.4
					031.76	3000	33.2
					032.76	3000	32.9
					033.64	3000	33.3
S1273	12.22	0.57	08:51:39.26	11:50:04.00	028.74	3000	34.6
					028.78	3000	34.6
					033.69	3000	34.7
					033.73	3000	34.8
S1275	12.56	0.59	08:51:37.43	11:50:05.40	009.74	3000	33.4
					011.77	1500	34.1
					031.76	3000	33.9
					032.76	3000	33.7
					033.64	3000	34.0
S1277	11.63	1.05	08:51:42.35	11:50:07.80	008.77	1500	34.6
					008.79	1500	34.3
S1279	10.55	1.12	08:51:28.98	11:50:33.00	007.76	1500	33.3
					007.78	1500	33.9
S1288	11.33	1.07	08:51:42.37	11:51:23.10	007.76	1500	33.4
					007.78	1500	34.0
S1293	12.09	1.01	08:51:39.42	11:51:45.90	028.74	3000	34.2
					028.78	3000	34.2
					033.69	3000	34.3
					033.73	3000	34.5

Table 1. Cont.

Sanders ID	V	(B-V)	α_{2000}	δ_{2000}	Julian Day + 2453000	Exposure time (sec)	v_{rad} (km.s ⁻¹)
S1305*	12.23	0.99	08:51:35.79	11:53:35.00	398.79	2580	34.3
					431.68	2580	34.2
S1319*	12.91	0.97	08:51:48.80	11:56:52.0	398.79	2580	34.4
					431.68	2580	34.3
S1323	12.83	0.78	08:51:35.43	11:57:56.80	028.74	3000	33.2
					028.78	3000	33.2
					033.69	3000	33.5
					033.73	3000	33.5
S1438*	12.89	0.82	08:52:11.35	11:45:37.50	398.79	2580	33.1
					431.68	2580	33.0
S1487*	12.63	0.64	08:52:04.81	11:58:28.80	398.79	2580	33.4
					431.68	2580	33.3
S1607*	12.62	0.56	08:52:21.45	11:50:41.70	398.79	2580	33.7
					431.68	2580	33.7
S2207*	12.65	0.62	08:51:32.47	11:47:52.50	398.79	2580	31.9
					431.68	2580	31.9
S2208	12.78	0.82	08:51:32.42	11:48:01.30	028.74	3000	33.0
					028.78	3000	33.0
					033.69	3000	33.1
					033.73	3000	33.1

VALD database (Kupka et al. 1999). These lines appear reasonably unblended throughout the spectral domain (4 200-8 000 Å) of the high-resolution spectra of the Sun and of Arcturus (Hinkle et al. 2000). For each line the central wavelength, excitation potential (χ_{exc}), and our value on $\log gf$ improved by an inverse solar and Arcturus analysis are presented in Table 6 (online material). The equivalent widths (EW) from the Sun and from Arcturus spectra (Hinkle et al. 2000) are also reported. They were measured with an automatic procedure using the DAOSPEC package (Stetson & Pancino 2008). In order to check our corrections on $\log gf$ values, we used our measured EWs to derive the FeI and FeII abundances for the Sun and for Arcturus. For the Sun, we adopted the following atmospheric parameters: $T_{\text{eff}} = 5777$ K (Neckel 1986), $\xi = 1.0$ km s⁻¹ (Ruedi et al. 1997), $\log g = 4.44$ (Allen 1973); and for Arcturus: $T_{\text{eff}} = 4300$ K, $\xi = 1.6$ km s⁻¹, $\log g = 1.8$ (Zoccali et al. 2004). The solar iron abundances we derived, $\log n(\text{FeI}) = 7.49 \pm 0.03$ dex and $\log n(\text{FeII}) = 7.48 \pm 0.04$ dex, agree well with the values of Asplund, Grevesse & Sauval (2005) and also with the value of the Fe II abundance found by Biémont et al. (1991). For Arcturus we found $\log n(\text{FeI}) = 7.02 \pm 0.05$ dex and $\log n(\text{FeII}) = 7.05 \pm 0.06$ dex, which agrees with determinations from Peterson et al. (1993) and from Carraro et al. (2004).

Then we estimated for our 27 sample stars the effective temperatures, microturbulent velocities, and stellar surface gravities by imposing an excitation equilibrium for the Fe I abundances, an equilibrium between the Fe I abundances and the equivalent widths, and a FeI/FeII ionization equilibrium as presented in Fig. 2 for the TO star S1275. The initial values adopted for the atmospheric parameters were the ones published in Canto Martins et al. (2007). In this previous work, the T_{eff} were estimated from photometry (Montgomery et al. 1993; Houdashelt et al. 2000), from the H_{α} and H_{β} lines and also the Fe I lines ratio in the Li region. The $\log g$ was estimated using evolutionary models. For the metallicities, the solar metallicity was adopted as a first guess and then adjusted by fitting the Fe I

lines for the Li region.

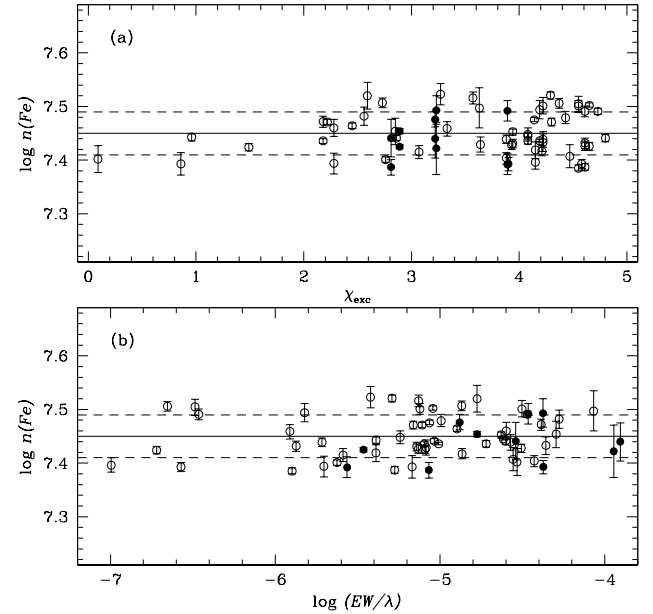


Fig. 2. Analysis of the turn-off star S1275 : (a) Fe lines excitation equilibrium. (b) relations between Fe abundances and equivalent widths. Open and filled circles represent the Fe I and Fe II lines, respectively. The solid line represents the mean iron abundance and the dashed lines represent the 1σ of the distribution.

With this method the metallicities $[\text{Fe}/\text{H}]$ were calculated for a solar abundance $\log n(\text{Fe})_{\odot} = 7.49$ (as derived here) and the $[\text{Fe}/\text{H}]$ errors are based on the standard deviations in the Fe I lines abundances only. The accuracies obtained on

atmospheric parameters are ± 70 K for T_{eff} , ± 0.2 dex for $\log g$ and ± 0.2 km s $^{-1}$ for ξ .

Table 2 provides the atmospheric parameters adopted to compute the synthetic spectra used to derive the projected rotational velocity ($v \sin i$) and A_{Li} for each star in our sample. To derive the projected rotational velocity, we used the same procedure as in de Medeiros et al. (2006). We convolved the resulting spectra (taking into account the instrumental profile of FLAMES-UVES) with a rotational profile to adjust the broadening observed on a group of Fe I lines in the Li region (6700–6720 Å). The $v \sin i$ values we measured (presented in Table 2) have an accuracy of ± 1.0 km s $^{-1}$.

Finally, the determination of A_{Li} was made by the best fit between observed and synthetic spectra, obtained on the Li line at 6707.78 Å. For each star, the total error on the Li abundance was estimated by computing the quadratic sum of errors induced by errors on individual parameters (T_{eff} , $\log g$, ξ , $[\text{Fe}/\text{H}]$, $v \sin i$) and also errors associated with the best-fit determinations. As discussed by De Laverny et al. (2003) and Lèbre et al. (2006), the main source of uncertainty in the abundances determinations is caused by errors in the T_{eff} determination. They have estimated that T_{eff} measurements with errors smaller than 200 K lead to errors smaller than 0.2 dex in the derived metallicity and lithium abundance. We made some tests, and the obtained errors are about the same as proposed in these previous studies. However, we found that errors in the parameters $\log g$ and ξ also influence the determination of the metallicity of the stars in our sample. We found that the errors obtained in $[\text{Fe}/\text{H}]$ caused by errors in $\log g$ are smaller than those measured when we analyse the errors in the metallicity caused by ξ . Taking into account the two sources of errors, we obtained a maximum error of 0.16 dex in $[\text{Fe}/\text{H}]$. In its last column, Table 2 also presents A_{Li} values and their accuracies. As an illustration we show in Fig. 3 a zoom on the Li region together with synthetic spectra for several values of A_{Li} for the TO star S1275.

The stellar parameters, microturbulent and rotational velocities and A_{Li} measured in this study are more accurate than the values produced by Canto Martins et al. (2007) because of the large number of Fe I and Fe II lines used in the characterization of the stellar sample.

2.3. Comparison with other spectroscopic studies

We compared the parameters we determined with previous spectroscopic studies available in the literature. Concerning the metallicity of M67 we found from our sample stars a mean metallicity for our evolved stars of $[\text{Fe}/\text{H}] = -0.05 \pm 0.04$. This value agrees very well with the lowest values from the literature as $[\text{Fe}/\text{H}] = -0.05$ (Canterna et al. 1986), $[\text{Fe}/\text{H}] = -0.07$ (Anthony-Twarog 1987), $[\text{Fe}/\text{H}] = -0.08$ (Friel & Jane 1991), $[\text{Fe}/\text{H}] = -0.09$ (Friel & Jane 1993), $[\text{Fe}/\text{H}] = -0.05$ (Shetrone & Sandquist 2000) and $[\text{Fe}/\text{H}] = -0.03$ (Tautvaišienė et al. 2000). However, other studies point to higher values for the mean metallicity of M67 as $[\text{Fe}/\text{H}] = 0.06$ (Nissen et al. 1987), $[\text{Fe}/\text{H}] = 0.04$ (Garcias Lopez et al. 1988), $[\text{Fe}/\text{H}] = 0.02$ (Friel & Boesgaard 1992), and recently, $[\text{Fe}/\text{H}] = 0.02 \pm 0.14$ (Yong et al. 2005), $[\text{Fe}/\text{H}] = 0.03 \pm 0.01$ (Randich et al. 2006, hereafter R06) and $[\text{Fe}/\text{H}] = 0.05 \pm 0.02$ (Pancino et al. 2010).

Table 2. Estimated atmospheric parameters for our sample stars. Rotational velocities and lithium abundances derived from our spectral synthesis analysis are also given. The identifiers (ID) are from Sanders (1977).

ID	T_{eff} (K)	$\log g$ (dex)	ξ (km.s $^{-1}$)	$[\text{Fe}/\text{H}]$ (dex)	$v \sin i$ (km.s $^{-1}$)	A_{Li}
Turn-off stars						
S1273	6159	4.01	1.86	-0.04±0.04	8.0	1.90±0.11
S1607	6127	3.81	1.77	-0.11±0.06	3.5	1.70±0.10
S1275	6050	4.00	1.64	-0.04±0.04	4.9	2.15±0.11
S1034	6020	3.90	1.94	-0.08±0.03	4.0	1.30±0.11
S2207	6000	3.90	1.62	-0.03±0.03	4.0	1.20±0.12
S1268	5996	3.86	1.75	-0.11±0.07	3.5	0.90±0.12
S1487	5940	3.81	1.67	-0.05±0.03	2.5	1.10±0.13
Subgiant stars						
S1242	5810	3.90	1.50	-0.04±0.06	6.1	2.70±0.13
S1323	5654	3.90	1.50	+0.03±0.04	3.3	<1.00
S1239	5644	3.80	1.41	+0.00±0.03	3.1	<0.80
S806	5461	3.80	1.25	+0.08±0.03	4.1	0.00±0.19
S2208	5429	3.90	1.24	+0.01±0.03	3.6	0.70±0.14
S1438	5420	3.80	1.27	-0.06±0.03	2.2	<0.00
S774	5240	3.70	1.20	-0.08±0.03	3.2	<0.00
Giant stars						
S1245	5170	3.61	1.19	-0.02±0.03	3.0	0.00±0.15
S1231	5130	3.60	1.12	-0.02±0.03	3.0	<0.10
S1319	5104	3.61	1.16	-0.07±0.03	3.0	<0.40
S1293	4970	3.30	1.32	-0.01±0.03	3.2	-0.20±0.22
S1305	4940	3.20	1.18	-0.08±0.03	2.8	< -0.20
S1254	4820	2.91	1.30	-0.03±0.04	3.0	< -0.40
S1277	4820	3.00	1.26	+0.01±0.05	3.0	< -0.40
S1279	4779	2.72	1.57	-0.01±0.08	2.5	-0.50±0.23
S1288	4773	2.90	1.32	-0.01±0.04	2.5	-0.20±0.21
S1074	4750	2.60	1.62	-0.07±0.04	2.5	-0.40±0.24
S1010	4748	2.60	1.58	-0.03±0.07	2.5	<0.00
S1016	4430	2.31	1.52	-0.05±0.05	2.0	-0.50±0.25
S978	4260	1.90	1.63	-0.15±0.06	2.0	-1.00±0.27

Table 3. Comparison for the star S1010 between atmospheric parameters from Tautvaišienė et al. (2000) (T00), Young et al. (2006) (Y05), and Pancino et al. (2010) (P10) and those derived in the present work.

Parameters	T00	Y05	P10	Our work
T_{eff} (K)	4730±100	4700±100	4650±100	4748±70
$\log g$	2.4±0.3	2.3±0.3	2.8±0.2	2.6±0.20
ξ (km s $^{-1}$)	1.6±0.3	1.34±0.2	1.3±0.1	1.58±0.20
$[\text{Fe}/\text{H}]$	-0.01±0.11	0.00±0.10	0.06±0.01	-0.03±0.07

Comparing some stars in our sample with other studies in greater detail, we have the star S1010 that was also studied by Tautvaišienė et al. (2000), Yong et al. (2005), and Pancino et al. (2010). Table 3 compares the values of the atmospheric parameters and metallicity measured for this star. Evidently the atmospheric parameters obtained in all studies agree well. However, we measured a lower metallicity compared to their results. One possible explanation for this is the higher solar iron abundance adopted by these studies ($\log n(\text{FeI}) = 7.54$ for Yong et al. 2006 and $\log n(\text{FeI}) = 7.50$ for Pancino et al. 2010). Another explanation is that both the superficial

Table 4. Comparison for S1034 and S1239 between atmospheric parameters from Randich et al. (2006) and lithium abundances from Randich et al. (2007) and those derived in the present work.

	S1034		S1239	
	Randich	Our work	Randich	Our work
T_{eff} (K)	5969 ± 70	6020 ± 70	5477 ± 70	5644 ± 70
$\log g$	4.0 ± 0.25	3.9 ± 0.20	3.8 ± 0.25	3.8 ± 0.20
ξ (km s $^{-1}$)	1.5 ± 0.15	1.94 ± 0.20	1.25 ± 0.15	1.41 ± 0.20
[Fe/H]	$+0.01 \pm 0.05$	-0.08 ± 0.03	$+0.02 \pm 0.03$	$+0.00 \pm 0.03$
A_{Li}	< 1.14	1.30 ± 0.11	1.12 ± 0.10	< 0.80

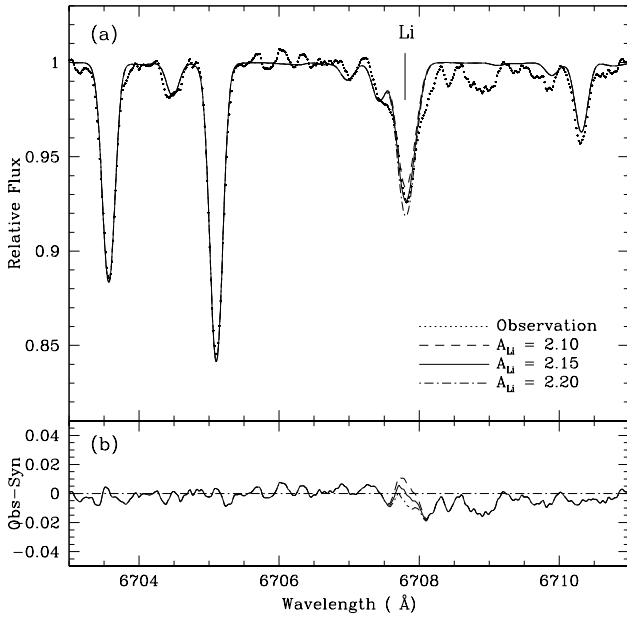


Fig. 3. Lithium line spectroscopic region of the turn-off star S1275: (a) observation (dotted line) and synthetic spectra computed with the atmospheric parameters listed in Table 2, and with $A_{\text{Li}} = 2.10, 2.15, 2.20$ dex (dashed, solid and dashed-dot lines respectively). The best synthetic spectrum is clearly the one computed with $A_{\text{Li}} = 2.15$. (b) Residual difference between synthetic and observed spectra.

gravity and the microturbulent velocity affect the metallicity of the star. In this case, as the value of ξ obtained in our study is higher than that obtained by Yong et al. (2005) and Pancini et al. (2010), this difference leads to errors on [Fe/H] smaller than 0.12 dex in S1010. This difference may also explain the low mean metallicity of M67 found in our study.

Two other targets, S1034 and S1239 (Fig. 4), were also included in the spectroscopic study of Randich et al. (2006). For these two objects, Table 4 provides the comparison of the stellar parameters between R06 and the present study. Both analyses appear to agree fairly well within the error bars for stellar parameters determination, even if we derive a lower metallicity for S1034 (but still consistent within the error bars) and a higher microturbulent velocity. However, the A_{Li} values present differences that may be explained by the adopted methodology

to compute the model atmosphere and synthetic spectra.

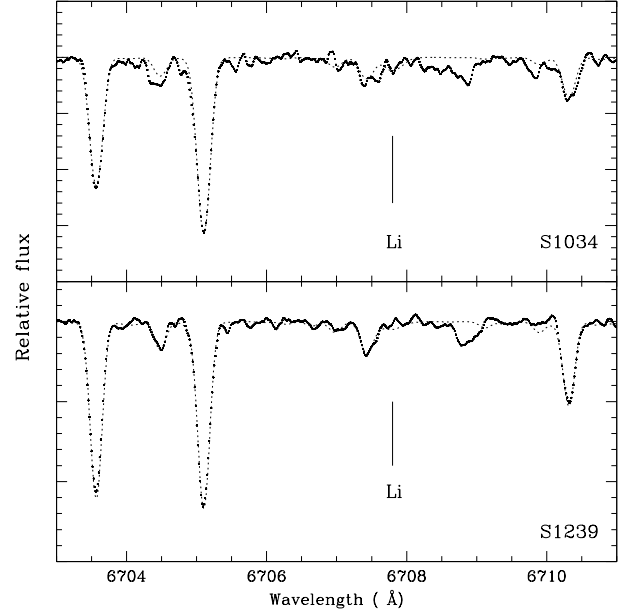


Fig. 4. Li region of the stars S1034 and S1239, which were also studied by Randich et al. (2006). Observations are represented with a dotted line and synthetic spectra by a dashed line. The vertical line indicates the Li feature at 6707.78 Å.

Finally, our rotational velocities ($v \sin i$) agree well with the results obtained by Melo et al. (2001) on evolved stars of M67. Moreover our study statistically extends the number of M67 evolved stars with measured $v \sin i$. In this way, our efforts complement the existing values of atmospheric parameters and $v \sin i$ values for M67 objects, and can assist studies that are mainly dedicated to the evolution of the angular momentum in the open cluster M67.

Up to date, as mentioned in different studies (Pilachowski et al. 1988, Balachandran 1995), subgiant and giant stars in M67 show no significant A_{Li} , which points to a severe Li depletion after the TO. For unevolved stars of M67, Jones et al. (1999) and Randich et al. (2002, 2007) show a large dispersion on the A_{Li} . Balachandran (1995) also studied the Li abundance in M67 evolved stars, but only upper limits were estimated. In this context, the analysis we performed on our sample complements the previous observational studies mainly devoted to stars of M67 near the TO. Our data present the same dispersion as established by Jones et al. (1999) and Randich et al. (2002 and 2007) and shows a gradual decrease of A_{Li} for stars cooler than 5500 K (see Fig. 7, next section). The present result points to a depletion of Li in excess to standard predictions as pointed out by Pasquini et al. (1997).

3. Connecting the Li abundances and the rotational velocities

The lithium abundances derived for our stars clearly indicate that this element has been depleted at their surface already during the

main sequence evolution. In an attempt to consistently explain the evolution of both the lithium abundances and the rotational velocities, we computed a grid of stellar evolution models with rotation and compared the predictions to our sample.

3.1. Stellar evolution models with rotation

We computed a grid of stellar evolution models in the mass range $1.30 M_{\odot}$ to $1.37 M_{\odot}$ (see Table 5) including rotation, microscopic diffusion, and thermohaline mixing (as described in Charbonnel & Zahn 2007) using STAREVOL V3.00 (Siess 2006,; Siess et al. 2008; Decressin et al. 2009). We used the solar abundances given by Asplund et al. (2005) as a reference for our stellar evolution models, and the corresponding opacities were generated with the OPAL Opacity code (Iglesias & Rogers 1996)¹. Convective zones are defined using the Schwarzschild criterion and the mixing length formalism with an adopted mixing length parameter $\alpha_{\text{MLT}} = 1.78$ that was calibrated on the Sun. The models have a metallicity of $[\text{Fe}/\text{H}] = -0.03$, which translates into a metal content $Z = 0.01148$. The initial helium mass fraction $Y_{\text{ini}} = 0.2688$ was calibrated for the solar model. The initial lithium content is set to $A_{\text{Li}} = 3.20^2$. Mass loss is included in our models from the ZAMS and beyond following Reimers (1975). Microscopic diffusion (gravitational settling) of chemical species is accounted for using the approximation of Paquette et al. (1986) for the microscopic diffusion coefficient and the expressions given by Montmerle & Michaud (1976) for the microscopic diffusion velocity. We adopt the Maeder & Zahn (1998) formalism to account for the transport of angular momentum and of chemical species by meridional circulation and shear-induced turbulence in the models. The formalism and its introduction in STAREVOL are described at length in Palacios et al. (2003, 2006), and we refer the reader to these papers for further details. Let us nonetheless recall that we use the prescription from Zahn (1992) for the horizontal turbulent diffusion coefficient D_h with $C_h = 1.0$. We also assume that convective regions rotate as solid bodies. For those models with equatorial velocity at the ZAMS of about 19 km.s^{-1} , we assume angular momentum losses associated with a magnetic torque as described by Kawaler (1988):

$$\left(\frac{dJ}{dt}\right) = -K\Omega^3 \left(\frac{R}{R_{\odot}}\right)^{1/2} \left(\frac{M}{M_{\odot}}\right)^{-1/2} \quad (\Omega < \Omega_{\text{sat}}) \quad (1)$$

$$\left(\frac{dJ}{dt}\right) = -K\Omega\Omega_{\text{sat}}^2 \left(\frac{R}{R_{\odot}}\right)^{1/2} \left(\frac{M}{M_{\odot}}\right)^{-1/2} \quad (\Omega \geq \Omega_{\text{sat}}). \quad (2)$$

The parameter K in Kawaler's law is related to the magnitude of the magnetic field strength, and $\Omega_{\text{sat}} = 14\Omega_{\odot}$ following Bouvier et al. (1997). Lacking observational data on the ZAMS to constrain the evolution of angular momentum of our sample stars, we use the $v \sin i$ derived by Melo et al. (2001) for main-sequence stars of M67 as a guideline to calibrate the braking. For masses 1.30 to $1.37 M_{\odot}$ we adopt $K = 8 \times 10^{29}$.

We checked that a model of $1.25 M_{\odot}$ including microscopic diffusion, no rotation, and a mixing length parameter calibrated for the Sun reaches the turn-off at 3.75 Gyr, in fair agreement with the value obtained by Michaud et al. (2004), who used a

more detailed treatment for microscopic diffusion and radiative forces. Below we will therefore consider an age of 3.7 Gyr for M67 and all discussed predictions will refer to values obtained when the models reach this age.

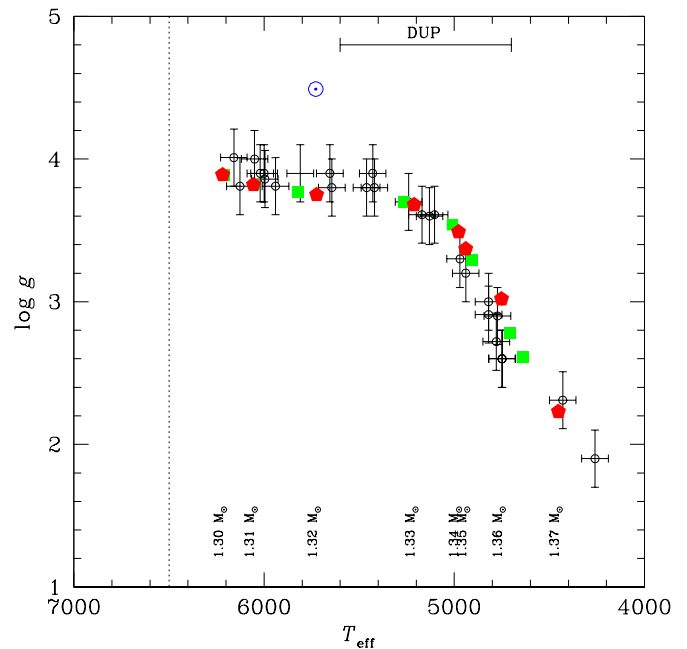


Fig. 5. $\log g$ versus T_{eff} for our sample of stars, represented by black circles. Values at 3.7 Gyr for the rotating models with and without angular momentum extraction are represented by filled red pentagons and filled green squares respectively. The dotted line indicates the turn-off (TO) position and the location of the first DUP is also indicated.

Table 5 presents the results of our modelling in terms of effective temperature and gravity, luminosity, equatorial velocity, and lithium abundance at the ZAMS, the turn-off (e.g. TO) and 3.7 Gyr (e.g. M67). Models with and without braking have an initial angular momentum of about 5.2×10^{49} and $3.2 \times 10^{49} \text{ g.cm}^2.\text{s}^{-1}$ respectively.

3.2. Evolutionary status and rotation

Our choice of masses for the models computed are based on the $1.3 M_{\odot}$ turn-off mass suggested by Michaud et al. (2004) for their 3.7 Gyr best-fitting isochrone to the M67 colour-magnitude diagram, and taking into account that our sample includes subgiant and giant stars that should be more massive. Figure 5 shows the surface gravity as a function of temperature for our sample stars together with our models at the age of 3.7 Gyr. Both types of models, whether they are slow or moderate rotators on the ZAMS, fall among the data points. The data are well reproduced by rotating models that have passed the turn-off (see Table 5), and that have initial masses between $1.30 M_{\odot}$ and $1.37 M_{\odot}$.

Figure 6 presents the rotation velocity $v \sin i$ of our data versus temperature and overplotted are the corresponding $v \sin i$ from our models at 3.7 Gyr. The models have an actual equatorial rotation velocity higher than the values plotted

¹ The tables were generated using the web interface available at <http://opalopacity.llnl.gov/>

² This abundance is obtained using the solar meteoritic abundance given by Asplund et al. (2005) scaled down to the metallicity of M67.

Table 5. Characteristics of stellar evolution models with rotation. Effective temperature, surface gravity, luminosity, surface rotation velocity, lithium abundance, age, and associated evolutionary phase are given for models with initial masses between $1.30 M_{\odot}$ and $1.37 M_{\odot}$. In the last column, “M67” refers to the models predictions at the adopted age for the cluster of 3.7 Gyr. For each quantity, the values for models without ($K_K = 0$) and with ($K_K \neq 0$) magnetic braking on the ZAMS are indicated, the latter is shown in bold face.

mass (M_{\odot})	T_{eff} (K)		log g (dex)		L (L_{\odot})		v_{surf} (km/s)		A_{Li} (dex)		age (Gyr)		phase
	$K_K = 0$	$K_K \neq 0$	$K_K = 0$	$K_K \neq 0$	$K_K = 0$	$K_K \neq 0$	$K_K = 0$	$K_K \neq 0$	$K_K = 0$	$K_K \neq 0$	$K_K = 0$	$K_K \neq 0$	
1.30	6699	6701	4.37	4.37	2.75	2.75	12.05	18.9	3.18	3.18	4.48 10^{-2}	4.76 10^{-2}	ZAMS
	6439	6440	3.99	3.99	5.55	5.57	10.86	8.88	2.99	1.26	3.36	3.38	TO
	6212	6218	3.89	3.89	6.11	6.15	7.97	8.03	2.93	1.14	3.7	3.7	M67
1.31	6729	6729	4.36	4.36	2.85	2.85	11.92	18.87	3.18	3.18	4.50 10^{-2}	4.50 10^{-2}	ZAMS
	6457	6472	3.99	3.99	5.70	5.70	10.72	9.00	2.93	1.27	3.24	3.24	TO
	6050	6056	3.82	3.82	6.48	6.49	7.40	7.22	2.80	1.08	3.7	3.7	M67
1.32	6757	6758	4.36	4.36	2.95	2.96	11.88	18.90	3.18	3.18	4.26 10^{-2}	4.26 10^{-2}	ZAMS
	6476	6499	3.99	4.00	5.88	5.79	10.75	9.05	2.93	1.23	3.19	3.11	TO
	5824	5724	3.77	3.75	6.38	6.20	5.84	5.73	2.65	0.93	3.7	3.7	M67
1.33	6787	6787	4.36	4.36	3.06	3.06	12.09	18.92	3.17	3.18	3.88 10^{-2}	4.02 10^{-2}	ZAMS
	6479	6508	3.97	3.99	6.11	6.05	10.71	9.15	2.92	1.32	3.14	3.07	TO
	5266	5211	3.70	3.68	4.98	4.89	3.63	4.14	1.82	0.19	3.7	3.7	M67
1.34	6814	6808	4.35	4.35	3.16	3.17	12.09	18.97	3.17	3.17	3.66 10^{-2}	3.78 10^{-2}	ZAMS
	6502	6526	3.97	3.98	6.28	6.22	10.71	9.24	2.93	1.37	3.05	2.99	TO
	5010	4978	3.54	3.49	5.88	6.59	2.54	3.08	1.44	-0.15	3.7	3.7	M67
1.35	6841	6842	4.35	4.35	3.28	3.28	12.09	18.97	3.17	3.18	3.38 10^{-2}	3.56 10^{-2}	ZAMS
	6552	6544	3.98	3.98	6.43	6.41	10.90	9.33	2.93	1.38	2.94	2.91	TO
	4909	4940	3.29	3.37	9.86	8.35	1.88	2.73	1.30	-0.23	3.7	3.7	M67
1.36	6875	6877	4.34	4.34	3.34	3.34	12.23	19.33	3.17	3.17	2.95 10^{-2}	3.02 10^{-2}	ZAMS
	6559	6521	3.97	3.95	6.63	6.74	10.81	9.33	2.94	1.37	2.84	2.91	TO
	4709	4752	2.78	3.02	26.90	22.87	1.11	1.60	1.26	-0.37	3.7	3.7	M67
1.37	6898	6902	4.34	4.34	3.51	3.51	12.23	20.45	3.17	3.17	3.03 10^{-2}	2.98 10^{-2}	ZAMS
	6515	6555	3.94	3.95	6.95	6.88	10.40	9.87	2.93	1.15	2.88	2.82	TO
	4637	4453	2.61	2.23	37.87	76.04	0.94	0.91	1.03	-0.61	3.7	3.7	M67

here that were obtained by multiplying the values of Table 5 by $\frac{\pi}{4}$ following Chandrasekhar (1950). They mimic a mean $v \sin i$ associated to what can be considered a mean equatorial velocity given by stellar evolution models. The initial velocity and braking parameters (when relevant) were chosen to obtain surface velocities between 8 and 1 km.s^{-1} at 3.7 Gyr. For models with $v_{\text{ZAMS}} \approx 19 \text{ km.s}^{-1}$, the evolution of the surface rotation is driven by the radius changes as the star evolves, so that it essentially drops from the ZAMS to the upper RGB. The more massive of our models, which are also the more evolved, present the lowest surface rotation velocities, in agreement with the observations. The angular momentum lost by the wind at the evolutionary phases considered is accounted for, but is found to be negligible.

Concerning the models that undergo magnetic braking, the figure shows the result of our calibration of the braking parameter K . The extraction of angular momentum when using the Kawaler law is maximum when the model arrives on the ZAMS, because it is proportional to the surface angular velocity. By the time the model reaches the turn-off, it is efficiently slowed down and the surface rotation velocity has dropped by more than a factor of 2 as can be seen in Table 5. The evolution of v_{surf} on the subgiant and red giant branches is then dominated by the increase of the radius as for the other family of models.

Referring back to Talon & Charbonnel (2003), we note that our models at the age of the Hyades have effective tempera-

tures between 6700 K and 6950 K, and would thus lie on the hot side of the Li dip. The convective envelope on the main sequence is thus shallow, and internal gravity waves are not expected to efficiently transport angular momentum or to influence the transport of chemicals. On the contrary, based on Palacios et al. (2003), we expect rotational mixing (e.g. meridional circulation and shear induced mixing) to efficiently transport Li so that the abundances derived from observations are reproduced. Let us note that the stars of M67 that are presently on the main sequence are less massive than $1.30 M_{\odot}$, and probably lie on the cool side of the Li dip. Thus according to Talon & Charbonnel (2003), we should expect an efficient transport of both angular momentum and chemicals by internal gravity waves, which should therefore be taken into account if these stars were to be modelled.

3.3. Lithium as tracer of rotational mixing on the main sequence

After choosing the masses and calibrating the initial rotation parameters so that the gravity and the $v \sin i$ patterns as a function of effective temperature are well reproduced for our sample stars, we look at what is obtained for the lithium abundance. The results are presented in Fig. 7, where we plot the derived lithium abundances for our M67 sample and the abundances obtained for each of our models at 3.7 Gyr. Li abundances appear here as a clear separator between the two families of models we considered. Models that are slow rotators and do not undergo magnetic braking on the ZAMS are ruled

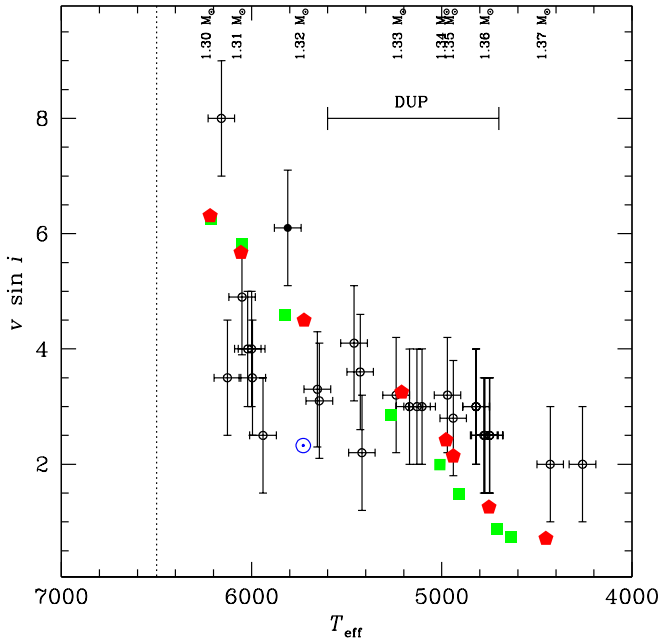


Fig. 6. $v \sin i$ versus T_{eff} for our sample of stars. Symbols are the same as in Fig. 5. The theoretical predictions here are mean $v \sin i$ and correspond to the v_{eq} values at 3.7 Gyr given in Table 5 multiplied by $\frac{\pi}{4}$. The filled dot is for S1242, which has been identified as a peculiar Li-rich subgiant in a previous work of ours (Canto Martins et al. 2006).

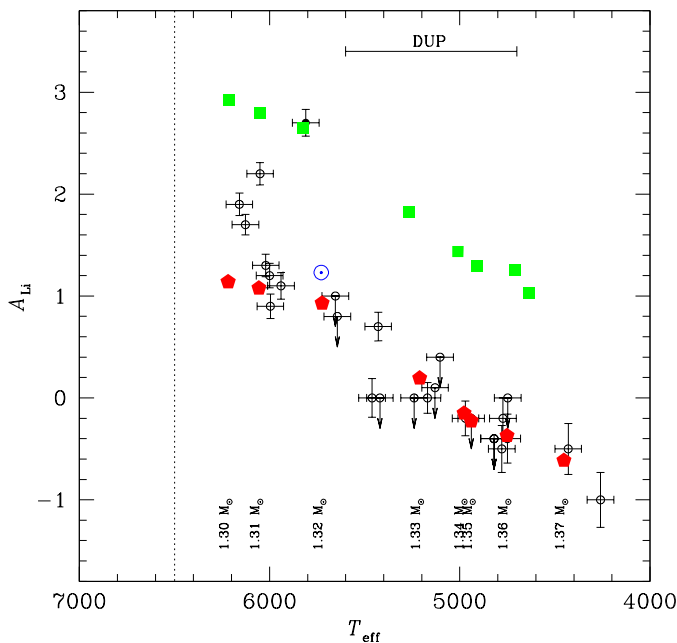


Fig. 7. A_{Li} versus T_{eff} for our sample of stars. Symbols are the same as in Figs. 5 and 6.

out. Actually the Li abundance evolves similarly to standard models in these models and lithium barely decreases at the surface during the main-sequence evolution, as can be seen from Table 5. On the contrary, models arriving on the ZAMS with mild rotation (about 19 km.s^{-1}) and undergoing magnetic

braking experience a reduction of the Li abundance by more than ≈ 1.6 dex during the main-sequence evolution. Afterwards, when the models evolve to the RGB, the 1st DUP further dilutes the Li of the envelope, and it almost disappears at the surface as can be seen from the 1.35, 1.36 and 1.37 M_{\odot} models. These models, presented as filled pentagons on Fig. 7, follow the trend obtained for our M67 sample and nicely reproduce the A_{Li} values derived from observations.

Without braking the angular velocity gradient below the convective envelope is shallow when the star is on the main sequence. As a consequence, the shear instability does not develop. Figure 8 presents the inner profile of A_{Li} and of the diffusion coefficient for chemicals ($D = D_{\text{mer.circ.}} + D_{\text{shear}} + D_{\text{micro}}$) as a function of the radial coordinate in the 1.33 M_{\odot} model while on main sequence ($t \approx 1.4$ Gyr). The solid lines refer to the model without braking, and we see that the diffusion coefficient is small in the region where Li is burned and the transport is strongly inefficient. Because the meridional circulation velocity also remains very slow (a few $10^{-8} \text{ cm.s}^{-1}$ at most), the transport of chemicals is dominated by the microscopic diffusion, which is a slow process ($D_{\text{mic}} \approx 100 \text{ cm}^2.\text{s}^{-1}$) leading to a small decrease of the surface lithium abundance, which would also be obtained in a non-rotating model with microscopic diffusion. On the other hand, the extraction of angular momentum associated with the magnetic braking leads to an increase of the angular velocity gradient in the stellar interior in a way that the shear instability sets in and the meridional circulation becomes stronger as the star is slowed down on the ZAMS. For the 1.33 M_{\odot} model, as can be seen in Fig. 8, the diffusion coefficient is two orders of magnitude higher than in the previous case just below the convective envelope, where the meridional circulation velocity is the highest ($\approx 10^{-5} \text{ cm.s}^{-1}$). It is also more than one order of magnitude larger in the region where Li is destroyed. As a result, as can be seen from the A_{Li} profile, lithium (and hydrogen) diffuses inwards, reducing the gradient around the radial coordinate $0.65 R_{\odot}$, and its surface abundance decreases. The depth of the DUP is not affected by rotation, and the subsequent decrease of A_{Li} at this stage is similar, whether angular momentum was extracted or not during the early evolution on the main sequence.

Let us emphasize that the lithium abundances obtained in our models with the adopted initial velocities and braking parameters fit the upper envelope of the values derived for the stars in our sample. The abundance determination lead only to upper limits for stars undergoing the DUP (in the range $T_{\text{eff}} \in [4700 \text{ K}, 5600 \text{ K}]$). However, we do not expect the actual values to be much lower than these limits considering that for the stars with $T_{\text{eff}} \approx 4500 \text{ K}$ in our sample, A_{Li} has been measured and is of about -0.5 dex. This value gives the lower limit for the post-DUP A_{Li} value. Because the shape of the A_{Li} vs T_{eff} pattern is well reproduced by our models, a slight adjustment of the rotation parameters so as to decrease more the Li on the main sequence would concomitantly bring down the values for more evolved models.

As explained above, we calibrated the braking parameters in our models to reproduce the evolution of the surface rotation velocity of stars beyond the turn-off in M67. This calibration depends on the equatorial rotation velocity adopted on the ZAMS. The models presented in Table 5 show that for $v_{\text{eq,ZAMS}} \approx 19 \text{ km.s}^{-1}$, the amount of angular momentum extraction needed to reach $v \sin i \approx 8.5 \text{ km.s}^{-1}$ at the turn-off following Melo et al. (2001) induces an internal transport of chemicals that results

in a decrease of the surface lithium abundance that agrees very well with our observational data. Considering the uncertainties on the equatorial rotation velocities of the now giant stars of M67 when they arrived on the ZAMS, one may now wonder what would happen if we had chosen a faster rotation on the ZAMS. We thus computed models of 1.30, 1.33 and 1.36 M_{\odot} with a larger initial content of angular momentum leading to $v_{eq,ZAMS} \approx 27.5 \text{ km.s}^{-1}$, and calibrated the magnetic braking parameter of Kawaler's law in order to reach $v \sin i$ values in the observed range when the models reach 3.7 Gyr. While the basic stellar parameters and the equatorial surface rotation velocities of these faster models resemble those presented in Table 5, the surface lithium abundance behaves very differently and is much lower at 3.7 Gyr. This is the direct consequence of a stronger shear mixing that develops in the stellar interior because of the stronger magnetic torque applied at the surface of the star during its early evolution on the main sequence. This test allows us to constrain the ZAMS equatorial velocity of stars in the mass range 1.30 M_{\odot} to 1.37 M_{\odot} of M67 considering that meridional circulation and shear turbulence are the main processes transporting lithium in this stars. We therefore exclude models with ZAMS equatorial velocities higher than 20 km.s^{-1} .

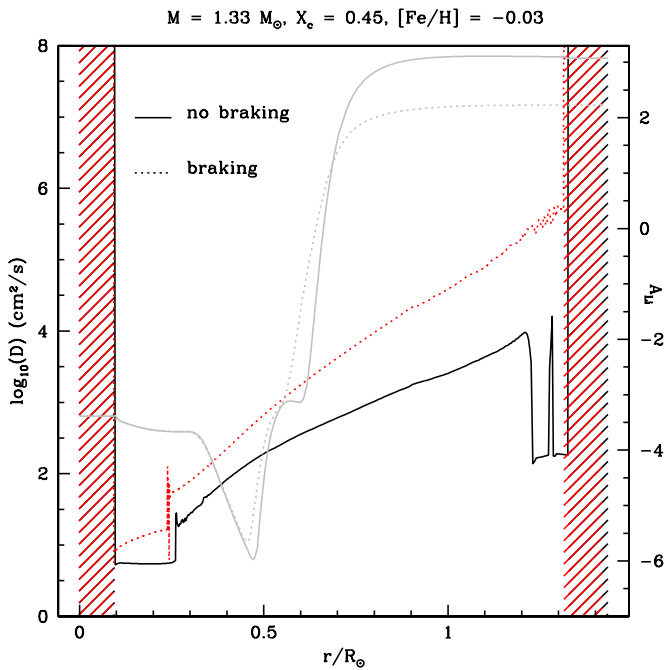


Fig. 8. Internal profiles of A_{Li} (grey) and of the logarithm of the total diffusion coefficient (black) as a function of the radial coordinate in rotating models with initial mass of 1.33 M_{\odot} with (dotted lines) and without (solid lines) braking. The profiles are shown for $t \approx 1.4$ Gyr, when the models are on the main sequence ($X_c \approx 0.46$). Left ordinates refer to the scale for the diffusion coefficient, while right ordinates represent the scale for the lithium abundance A_{Li} . Hatched regions represent convective zones.

4. Conclusions

We performed a spectroscopic analysis for a unique sample of 27 evolved stars of the old open cluster M67 following an evolutionary sequence from the turn-off to the Red Giant Branch. In this analysis we used a spectral synthesis procedure based

on MARCS model atmospheres to derive the stellar parameters (T_{eff} , $\log g$, [Fe/H]), microturbulent and rotational velocities, and the lithium abundance. The surface lithium content of the analysed stars follows a clear evolutionary pattern ranging from the turn-off to the Red Giant Branch. Our results reproduce the lithium abundance dispersion previously established for the M67 main-sequence stars and also confirm the well known gradual decrease of A_{Li} for T_{eff} below 5500 K. The lithium abundances derived for our sample stars clearly indicate that this element has been already depleted at the stellar surface during the main-sequence stage, which also points to a depletion in excess of standard predictions. The present study largely extends the number of evolved stars studied in M67. For the first time, it offers solid possibilities for an evolutionary study of different stellar parameters (A_{Li} and $v \sin i$) and also to test non-standard transport processes on homogeneous sample of turn-off and evolved stars of M67.

We tested the hypothesis that lithium and surface rotation evolution might be connected by comparing our data to the predictions of a set of stellar evolution models including the transport of matter and angular momentum by meridional circulation and shear-induced turbulence. It appears that these models (following Maeder & Zahn 1998 formalism for the transport of angular momentum) consistently reproduce the entire set of observational data when the evolution of angular momentum in the models includes an early phase of magnetic braking “à la Kawaler”, the efficiency of which is calibrated on the $v \sin i$ data available for main-sequence and turn-off stars of M67. This result is similar to what was also obtained by Smiljanic et al. (2010) for the open cluster IC 4651, and confirms the importance of rotation-induced mixing in determining light elements abundance patterns in low-mass stars in particular for those with initial masses larger than 1.30 M_{\odot} when at solar metallicity.

Acknowledgements. This work has been supported by continuous grants from CNPq Brazilian Agency (J.R. De Medeiros and J.D. do Nascimento Jr.) and by financial support from the french CNRS/INSU Programme National de Physique Stellaire (A. Lèbre, A. Palacios, O. Richard, P. De Laverny). B. L. Canto Martins acknowledges CAPES Brazilian Agency for a Ph.D. fellowship. The authors warmly thank Bertrand Plez and Thomas Masseron for their help on the use of MARCS models and *TurboSpectrum* routines, as well as for the molecular lists they provided.

References

- Allen, C. W. 1973, “Astrophysical Quantities”, 2nd ed., London: The Athlone Press
- Alvarez, R., & Plez, B. 1998, A&A, 330, 1109
- Anthony-Twarog, B. J. 1987, AJ, 93, 647
- Asplund, M., Grevesse, N., & Sauval, A. J. 2005, Cosmic Abundances as Records of Stellar Evolution and Nucleosynthesis, 336, 25
- Barklem, P., Piskunov, N., O’Mara, B.J. 2000a, A&AS, 142, 467
- Barklem, P., Piskunov, N., O’Mara, B.J. 2000b, A&A, 363, 1091
- Barklem, P., Piskunov, N. 2003, IAU Symp 210, E28
- Barklem, P., Aspelund-Johansson, J. 2005, A&A, 435, 373
- Balachandran, S. 1995, ApJ, 446, 203
- Bouvier, J., Forestini, M., & Allain, S. 1997, A&A, 326, 1023
- Burstein D., Faber S.M., Gonzalez J.J., 1986, AJ 91, 1130
- Biemont E., Baudoux M., Kurucz R., Ansbacher W., Pinnington E.H., 1991, A&A 249, 539
- Canterna, R., Geisler, D., Harris, H. C., Olszewski, E., Schommer, R. 1986 AJ, 92, 79
- Canto Martins, B. L., Do Nascimento J. D. Jr., de Medeiros J. R., Lèbre A., Richard O., de Laverny P., Melo C. H. F., 2007, International Journal of Modern Physics D, Vol. 16, 391
- Canto Martins, B. L., Lèbre, A., de Laverny, P., Melo, C. H. F., Do Nascimento, J. D., Jr., Richard, O., & de Medeiros, J. R. 2006, A&A, 451, 993
- Carraro, G., Bresolin, F., Villanova, S., Matteucci, F., Patat, F. et al. 2004, AJ, 128, 1676

- Carraro G., Girardi L., Bressan A., Chiosi C., 1996, *A&A* 305, 849
- Chandrasekhar, S., Münch, G. 1950, *ApJ*, 111, 142
- Charbonnel, C., & Zahn, J.-P. 2007, *A&A*, 467, L15
- Charbonnel C., Balachandran S.C., 2000, *A&A* 359, 563
- Charbonnel C., Talon S., 1999, *A&A* 351, 635
- Chaboyer B., Demarque P., Pinsonneault M.H., 1995, *ApJ* 441, 876
- De Laverny, P., do Nascimento, J. D., Jr., Lèbre, A., De Medeiros, J. R. 2003, *A&A*, 410, 937
- De Medeiros J.R., Silva J.R.P., do Nascimento J.D. Jr. et al., 2006, *A&A*, 458, 895
- Decressin, T., Mathis, S., Palacios, A., Siess, L., Talon, S., Charbonnel, C., & Zahn, J.-P. 2009, *A&A*, 495, 271
- Deliyannis, C. P., Pinsonneault M.H., 1997, *ApJ*, 488, 836
- D'Antona, F., Mateucci, F. 1991, *A&A* 248, 62
- Duncan D.K., 1981, *ApJ* 248, 651
- Fekel F.C., Balachandran S., 1993, *ApJ* 403, 708
- Friel, E. D., Janes, K. A. 1991, *ASPC*, 13, 569
- Friel, E. D., Boesgaard, A. M. 1992, *ApJ*, 387, 170
- Friel E. D., Janes K.A., 1993, *A&A* 267, 75
- Garcia Lopez, R. J., Rebolo, R., Beckman, J. E. 1988, *PASP*, 100, 1489
- Garcia Lopez R.J., Spruit H.C., 1991, *ApJ*, 377, 268
- Grevesse, N., & Sauval, A. J. 1998, *SSRv*, 85, 161
- Gustafsson, B., Edvardsson, B., Eriksson, K., Jorgensen U.G., Nordlund A., Plez B., 2008, *A&A* 486, 951
- Herbig G.H., 1965, *ApJ* 141, 588
- Hill, V., Plez, B., Cayrel, R., et al. 2002, *A&A*, 387, 560
- Hinkle, K., Wallace, L., Valenti, J., Harmer, D. 2000, *Visible and Near Infrared Atlas of the Arcturus Spectrum 3727–9300Å* (San Francisco: ASP Publisher)
- Houdashelt, M. L., Bell, R. A., Sweigart, A. V. 2000, *AJ*, 119, 1448
- Iglesias C. A. & Rogers F. J. , 1996, *ApJ*, 464, 943
- Jones, B. F., Fischer, D., Soderblom, D. R. 1999, *AJ*, 117, 330
- Kawaler, S. D. 1988, *ApJ*, 333, 236
- Kupka, F., Piskunov, N. E., Ryabchikova, T. A., Stempels, H. C., Weiss, W. W. 1999, *A&AS*, 138, 119
- Lèbre, A., De Laverny, P., Do Nascimento, J. D., Jr., de Medeiros, J. R. 2006, *A&A*, 450, 1173
- Maeder, A., & Zahn, J.-P. 1998, *A&A*, 334, 1000
- Melo, C. H. F., Pasquini, L., De Medeiros, J. R. 2001, *A&A*, 375, 851
- Michaud, G., 1986, *ApJ* 302, 650
- Michaud, G., Richard, O., Richer, J., Vandenberg, D. A. 2004, *ApJ*, 606, 452
- Momany, Y., Vandame, B., Zaggia, S., Mignani, R. P., da Costa, L. et al. 2001, *A&A*, 379, 436
- Montalba J., Schatzmann E., 2000, *A&A*, 354, 943
- Montgomery, K. A., Marschall, L. A., Janes, K. A. 1993, *AJ*, 106, 181
- Montmerle, T., & Michaud, G. 1976, *ApJS*, 31, 489
- Neckel H., 1986, *A&A* 159, 175
- Nissen, P. E., Twarog, B. A., Crawford, D. L. 1987, *AJ*, 93, 634
- Palacios, A., Talon, S., Charbonnel, C., Forestini, M. 2003, *A&A* 399, 603
- Palacios, A., Charbonnel C., Talon, S. & Siess, L. 2006, *A&A*, 453, 261
- Pallavicini R., Cerruti-Sola M., Duncan D.K., 1987, *A&A*, 174, 116
- Pancino, E., Carrera, R., Rossetti, E., Gallart, C. 2010, *A&A*, 511, 56
- Paquette, C., Pelletier, C., Fontaine, G., & Michaud, G. 1986, *ApJS*, 61, 177
- Pasquini, L., Avila, G., Blecha, A., et al. 2002, *The Messenger*, 110, 1
- Pasquini, L., Randich, S., Pallavicini, R. 1997, *A&A*, 325, 535
- Peterson, R. C., Dalle Ore, C. M., Kurucz, R. L. 1993, *ApJ*, 404, 333
- Pilachowski, C., Saha, A, Hobbs, L. M. 1988, *PASP*, 100, 474
- Pinsonneault, M. H., 1997, *ARA&A* 35, 557
- Pinsonneault M.H., Deliyannis C., Demarque P., 1991, *ApJ* 367, 239
- Pinsonneault M.H., Kawaler S.D., Demarque P., 1990, *ApJS* 74, 501
- Plez, B. 1998, *A&AS* 337, 495
- Randich S., Primas F., Pasquini, L., Sestito P., Pallavicini R., 2007, *A&A*, 469, 163
- Randich S., Sestito P., Primas F., Pallavicini R., Pasquini L., 2006, *A&A*, 450, 557
- Randich S., Primas F., Pasquini L., Pallavicini R. 2002, *A&A*, 387, 222
- Randich S., Giampapa M.S., Pallavicini R. 1994, *A&A*, 283, 893
- Recio-Blanco, A., de Laverny, P. 2007, *A&A*, 461, 13
- Reeves, H., Fowler, W., Hoyle, F. 1970, *Nature*, 226, 227
- Rüedi, I., Solanki, S. K., Mathys, G., Saar, S. H. 1997, *A&A*, 318, 429
- Reimers, D. 1975, *Memoires of the Société Royale des Sciences de Liège*, 8, 369
- Sanders, W. L. 1977, *A&AS*, 27, 89
- Sarajedini A., Dotter A., Kirkpatrick A., 2009, *ApJ* 698, 1872
- Schatzmann E., Balgin A., 1991, *A&A* 249, 125
- Shetrone M., Sandquist E., 2000, *AJ* 120, 1913
- Siess, L., & Arnould, M. 2008, *A&A*, 489, 395
- Siess, L. 2006, *A&A*, 448, 717
- Sills, A., & Deliyannis, C. P. 2000, *ApJ*, 544, 944
- Skumanich A., 1972, *ApJ* 171, 565
- Smiljanic R., Pasquini L., Charbonnel C., Lagarde N., 2010, *A&A* 510, A50
- Soderblom D.R., 1983, *ApJS*, 53, 1
- Spite F., Spite M., 1982, *A&A*, 115, 357
- Stetson P. B., Pancino E., 2008, *PASP* 120, 1332
- Talon, S., Charbonnel, C. 2003, *A&A* 405, 1025
- Talon, S., & Charbonnel, C. 1998, *A&A*, 335, 959
- Tautvaišiene, G., Edvardsson, B., Tuominen, I., Ilyin, I. 2000, *A&A*, 360, 499
- VandenBerg D. A., Stetson P.B., 2004, *PASP* 116, 997
- Yong, D., Carney, B. W., Teixeira de Almeida, M. L. 2005, *AJ*, 130, 597
- Zahn, J.-P. 1992, *A&A*, 288, 829
- Zoccali M., Barbuy B., Hill V. et al., 2004, *A&A* 423, 507

Table 6. Iron line list used for curve of growth and spectral synthesis, with atomic parameters, corrected oscillator strengths and solar and Arcturus equivalent width measurements.

Element	λ (Å)	χ_{exc} (eV)	$\log gf$	EW_{\odot} (mÅ)	EW_{Arc} (mÅ)
Fe I	5036.919	3.017	-2.938	24.3	64.8
Fe I	5044.211	2.851	-2.128	70.3	117.8
Fe I	5054.643	3.640	-2.051	38.7	65.0
Fe I	5228.377	4.220	-1.115	57.5	83.8
Fe I	5242.493	3.634	-1.007	81.2	112.8
Fe I	5247.051	0.087	-4.936	66.0	175.6
Fe I	5321.108	4.434	-1.301	40.0	59.2
Fe I	5322.041	2.279	-2.953	60.7	115.1
Fe I	5326.143	3.573	-2.211	35.8	69.9
Fe I	5373.709	4.473	-0.830	60.7	76.9
Fe I	5386.330	4.154	-1.740	31.1	51.3
Fe I	5522.444	4.209	-1.450	43.4	62.0
Fe I	5543.936	4.217	-1.080	62.0	81.8
Fe I	5618.633	4.209	-1.316	50.5	69.5
Fe I	5638.262	4.220	-0.810	75.1	97.3
Fe I	5701.547	2.559	-2.276	82.3	142.4
Fe I	5705.465	4.301	-1.492	38.4	57.8
Fe I	5741.848	4.256	-1.674	32.0	51.5
Fe I	5775.081	4.220	-1.188	59.2	81.1
Fe I	5778.453	2.588	-3.510	23.0	73.0
Fe I	5806.725	4.607	-0.975	52.0	68.1
Fe I	5811.914	4.143	-2.390	10.7	23.5
Fe I	5852.219	4.548	-1.260	39.4	—
Fe I	5853.148	1.485	-5.200	7.3	62.8
Fe I	5855.077	4.608	-1.583	21.5	34.1
Fe I	5856.088	4.294	-1.615	33.5	54.5
Fe I	5858.778	4.220	-2.245	12.6	27.2
Fe I	5916.247	2.453	-2.994	55.2	112.9
Fe I	5927.789	4.652	-1.105	41.7	54.1
Fe I	5934.657	3.928	-1.225	71.9	101.8
Fe I	5956.694	0.859	-4.630	52.5	148.9
Fe I	5976.777	3.943	-1.365	65.0	101.8
Fe I	5987.066	4.795	-0.556	64.1	79.2
Fe I	6003.014	3.881	-1.140	79.5	107.8
Fe I	6019.362	3.573	-3.280	5.2	17.8
Fe I	6027.051	4.076	-1.190	9.4	89.2
Fe I	6054.070	4.371	-2.245	9.4	17.9
Fe I	6056.005	4.733	-0.490	69.7	81.7
Fe I	6079.009	4.652	-1.050	45.7	—
Fe I	6105.128	4.548	-2.000	11.1	21.2
Fe I	6120.249	0.915	-5.910	5.3	66.7
Fe I	6151.618	2.176	-3.359	50.6	113.9
Fe I	6157.728	4.076	-1.270	61.7	92.7
Fe I	6159.373	4.607	-1.920	12.0	—
Fe I	6165.358	4.143	-1.535	44.9	66.9
Fe I	6180.204	2.727	-2.736	54.7	108.5
Fe I	6187.988	3.943	-1.735	46.3	74.2
Fe I	6226.736	3.883	-2.145	28.1	—
Fe I	6229.226	2.845	-2.970	37.2	86.0
Fe I	6240.646	2.223	-3.353	48.9	—
Fe I	6265.136	2.176	-2.700	83.2	160.2
Fe I	6270.225	2.858	-2.670	51.9	102.2
Fe I	6271.277	3.332	-2.776	23.4	58.3
Fe I	6297.795	2.223	-2.871	73.4	143.3
Fe I	6315.809	4.076	-1.683	40.9	66.9
Fe I	6380.743	4.186	-1.396	50.6	—
Fe I	6392.539	2.279	-3.990	17.5	—
Fe I	6498.939	0.958	-4.701	46.1	144.3
Fe I	6574.228	0.990	-4.940	33.1	125.7
Fe I	6575.018	2.588	-2.765	64.6	—
Fe I	6581.208	1.485	-4.730	20.2	97.5
Fe I	6608.026	2.279	-4.010	17.3	74.5
Fe I	6627.543	4.548	-1.560	27.2	42.1
Fe I	6646.932	2.608	-4.015	9.3	50.0
Fe I	6653.851	4.154	-2.470	9.9	23.6
Fe I	6699.140	4.593	-2.179	8.3	15.2

Table 6. Cont.

Element	λ (Å)	χ_{exc} (eV)	$\log gf$	EW_{\odot} (mÅ)	EW_{Arc} (mÅ)
Fe I	6703.568	2.758	-3.080	38.5	89.5
Fe I	6704.480	4.217	-2.650	6.4	14.0
Fe I	6705.102	4.607	-1.136	46.3	61.0
Fe I	6707.420	4.610	-2.245	6.3	—
Fe I	6710.318	1.485	-4.865	16.3	89.2
Fe I	6713.045	4.607	-1.553	24.2	—
Fe I	6713.190	4.143	-2.475	10.2	21.3
Fe I	6713.740	4.795	-1.465	21.4	28.4
Fe I	6715.382	4.607	-1.535	26.5	—
Fe I	6716.233	4.580	-1.875	15.3	—
Fe I	6725.357	4.103	-2.250	17.7	35.4
Fe I	6726.665	4.607	-1.129	47.1	59.9
Fe I	6733.149	4.638	-1.485	26.9	38.2
Fe I	6739.520	1.557	-4.929	12.4	76.9
Fe I	6752.705	4.638	-1.314	35.7	54.7
Fe I	6786.858	4.191	-1.950	25.3	44.7
Fe I	6806.845	2.727	-3.167	35.2	89.7
Fe I	6810.261	4.607	-1.068	49.0	65.1
Fe I	6971.932	3.018	-3.475	12.8	47.4
Fe I	7112.167	2.990	-3.035	31.6	31.6
Fe I	7189.150	3.071	-2.761	36.5	36.5
Fe I	7401.680	4.186	-1.625	39.9	39.9
Fe I	7710.362	4.220	-1.231	62.2	62.2
Fe I	7723.204	2.279	-3.542	37.8	37.8
Fe I	7941.087	3.274	-2.550	41.9	41.9
Fe II	4993.354	2.807	-3.772	38.0	—
Fe II	5100.627	2.807	-4.260	17.3	37.4
Fe II	5132.664	2.807	-4.130	21.5	16.8
Fe II	5136.794	2.844	-4.440	10.0	—
Fe II	5197.570	3.230	-2.450	74.5	71.1
Fe II	5234.625	3.221	-2.390	78.3	78.8
Fe II	5264.805	3.230	-3.205	44.9	38.8
Fe II	5325.553	3.221	-3.310	42.0	38.6
Fe II	5414.070	3.221	-3.677	25.5	22.5
Fe II	6084.103	3.199	-3.808	20.3	20.9
Fe II	6369.458	2.891	-4.253	18.1	19.2
Fe II	6416.923	3.892	-2.790	38.1	35.4
Fe II	6456.383	3.903	-2.075	60.6	46.7
Fe II	7224.475	3.889	-3.317	19.1	19.1